European Journal of Mechanics A/Solids 48 (2014) 38–47

Contents lists available at ScienceDirect

European Journal of Mechanics A/Solids

journal homepage: www.elsevier.com/locate/ejmsol

The Living Heart Project: A robust and integrative simulator for human heart function

Brian Baillargeon [a], Nuno Rebelo [a], David D. Fox [b], Robert L. Taylor [c], Ellen Kuhl [d,*]

[a] Dassault Systèmes Simulia Corporation, Fremont, CA 94538, USA
[b] Dassault Systèmes Simulia Corporation, Providence, RI 02909, USA
[c] Department of Civil and Environmental Engineering, University of California at Berkeley, Berkeley, CA 94720, USA
[d] Departments of Mechanical Engineering, Bioengineering, and Cardiothoracic Surgery, Stanford University, Stanford, CA 94305, USA

ARTICLE INFO

Article history:
Received 22 February 2014
Accepted 7 April 2014
Available online 24 April 2014

Keywords:
Electro-mechanics
Cardiac mechanics
Abaqus

ABSTRACT

The heart is not only our most vital, but also our most complex organ: Precisely controlled by the interplay of electrical and mechanical fields, it consists of four chambers and four valves, which act in concert to regulate its filling, ejection, and overall pump function. While numerous computational models exist to study either the electrical or the mechanical response of its individual chambers, the integrative electro-mechanical response of the whole heart remains poorly understood. Here we present a proof-of-concept simulator for a four-chamber human heart model created from computer topography and magnetic resonance images. We illustrate the governing equations of excitation–contraction coupling and discretize them using a single, unified finite element environment. To illustrate the basic features of our model, we visualize the electrical potential and the mechanical deformation across the human heart throughout its cardiac cycle. To compare our simulation against common metrics of cardiac function, we extract the pressure–volume relationship and show that it agrees well with clinical observations. Our prototype model allows us to explore and understand the key features, physics, and technologies to create an integrative, predictive model of the living human heart. Ultimately, our simulator will open opportunities to probe landscapes of clinical parameters, and guide device design and treatment planning in cardiac diseases such as stenosis, regurgitation, or prolapse of the aortic, pulmonary, tricuspid, or mitral valve.

1. Motivation

The human heart beats about 100,000 times daily, 30 million times annually, and 2.5 billion times in an average lifetime (Berne and Levy, 2001). Only marginally larger than a fist, it is capable of pumping 7000 liters of blood per day, 2.5 million per year, and 200 million throughout an individual's life span (Kumar et al., 2005). Fig. 1 shows an anatomic model of the human heart created from computer tomography and magnetic resonance images (Zygote Media Group and Inc., 2013). Our heart consists of four chambers, the left and right atria and the left and right ventricles, connected by four valves. Fig. 2 illustrates the four valves, the tricuspid and mitral valves, which connect the right and left atria to the right and left ventricles, and the pulmonary and aortic valves, which connect the right and left ventricles to the pulmonary and systemic circulation (Zygote Media Group and Inc., 2013). The coordinated opening and closing of these valves regulates the filling of the chambers, while the interplay of electrical and mechanical fields controls their proper ejection. Disturbed valvular opening, stenosis, disturbed closing, regurgitation, disturbed electrical signals, arrhythmias, and reduced mechanical function, heart failure, can have devastating physiological consequences (Braunwald, 1997). Modeling the interplay between electrical excitation and mechanical contraction provides insight into these complex phenomena and holds the potential to improve treatment for the millions of people affected by cardiac disease (Hunter et al., 2003).

Heart disease is the primary cause of death in the industrialized nations, claiming more than 16 million lives worldwide every year (American Heart Associatio, 2014). The origin of the heart disease is often local: Fibrillation and myocardial infarction are classical examples of local electrical and mechanical dysfunction. However, irrespective of its nature and initial location, cardiac disease almost always progresses to affect the entire heart, and eventually impairs the electrical and mechanical function of all four chambers (Kumar

* Corresponding author.
E-mail address: ekuhl@stanford.edu (E. Kuhl).

http://dx.doi.org/10.1016/j.euromechsol.2014.04.001

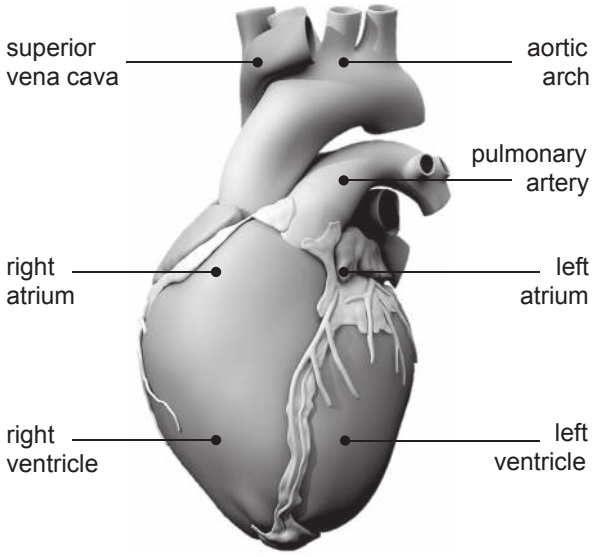

Fig. 1. Anatomic model of the human heart created from computer tomography and magnetic resonance images. The model displays the characteristic anatomic features: The aortic arch, the pulmonary artery, and the superior vena cava; the two upper chambers, the left and right atria; and the two lower chambers, the left and right ventricles; adopted with permission from (Zygote Media Group and Inc., 2013).

et al., 2005). To understand the fundamental pathologies of different forms of cardiac disease and optimize their treatment options, it is critical to model the entire heart as a whole, rather than studying the diseased subsystem in complete isolation (Trayanova, 2011).

To date, numerous computational models exist to simulate the behavior of the left ventricle (Eriksson et al., 2013; Klepach et al., 2012; Lee et al., 2013; Rossi et al., 2014), fewer model exist to simulate both the ventricles (Berberoglu et al., 2014; Hurtado and Henao, 2014; Kotikanyadanam et al., 2010; Trayanova et al., 2011),

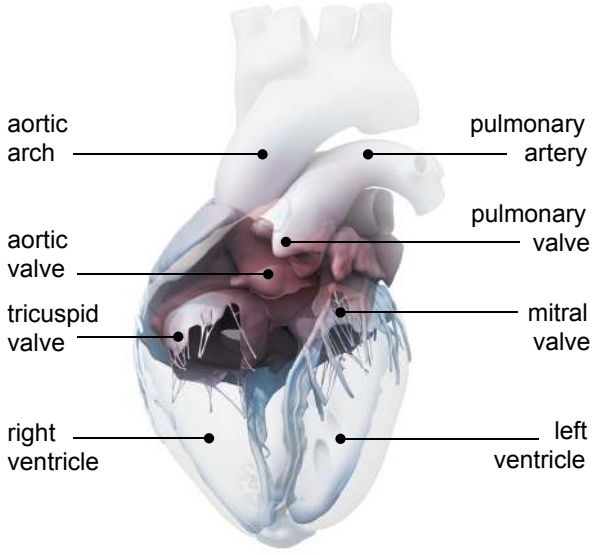

Fig. 2. Circulatory model of the human heart created from computer tomography and magnetic resonance images. The model displays the characteristic circulatory features: The tricuspid and mitral valves, which connect the right and left atria to the right and left ventricles; and the pulmonary and aortic valves, which connect the right and left ventricles to the pulmonary and systemic circulation; adopted with permission from (Zygote Media Group and Inc., 2013).

and only very few models exist to simulate the human heart with all four chambers (Gonzales et al., 2013; Trayanova, 2011). Creating whole heart models remains challenging because the atrial wall is about an order of magnitude thinner than the ventricular wall. In addition, the atria are typically entangled and their geometry can be quite complex (Gonzales et al., 2013). This not only complicates image segmentation, but also atrial discretization and meshing. Here we create a finite element model of the whole heart on the basis of existing anatomic and circulatory models illustrated in Figs. 1 and 2. This allows us to model all four chambers as electrically excitable, deformable, hyperelastic, electroactive bodies connected via in- and out-flow conditions of viscous resistance type.

The remainder of this manuscript is organized as follows: In Section 2, we summarize the continuum model of electro-mechanical coupling based on the kinematic equations, the balance equations, and the constitutive equations. In Section 3, we illustrate our computational model, based on the strong and weak forms of the governing equations, their temporal and spatial discretizations, their linearizations, and the handling of their internal variables. In Section 4, we document the creation of our human heart model including the solid model, the finite element model, the muscle fiber model, the fluid model, and a summary of all model parameters. In Section 5 we illustrate the simulation of an entire cardiac cycle. We close with a discussion of the results, the limitations, an outlook, and some conclusions in Section 6.

2. Continuum model

We illustrate the continuum model of electro-mechanical coupling by briefly summarizing the kinematic equations, the balance equations, and the constitutive equations of excitation–contraction coupling.

2.1. Kinematic equations

To characterize the kinematics of finite deformation, we introduce the deformation map $\boldsymbol{\varphi}$, which maps particles $\boldsymbol{X}$ from the undeformed reference configuration to particles $\boldsymbol{x} = \boldsymbol{\varphi}(\boldsymbol{X},t)$ in the deformed configuration (Holzapfel, 2000). Its derivative with respect to the undeformed coordinates $\boldsymbol{X}$ defines the deformation gradient,

$$\boldsymbol{F} = \overline{\boldsymbol{F}}\cdot\boldsymbol{F}^{\mathrm{vol}} = \nabla\boldsymbol{\varphi}, \tag{1}$$

which we decompose multiplicatively into a volumetric part $\boldsymbol{F}^{\mathrm{vol}}$ and an isochoric part $\overline{\boldsymbol{F}}$,

$$\boldsymbol{F}^{\mathrm{vol}} = J^{1/3}\boldsymbol{I} \quad \text{and} \quad \overline{\boldsymbol{F}} = J^{-1/3}\boldsymbol{F}, \tag{2}$$

with Jacobians $J^{\mathrm{vol}}=\det(\boldsymbol{F}^{\mathrm{vol}})=\det(\boldsymbol{F})=J$ and $\overline{J} = \det(\overline{\boldsymbol{F}}) = 1$. We can then introduce the isochoric right Cauchy-Green deformation tensor,

$$\overline{\boldsymbol{C}} = \overline{\boldsymbol{F}}^{\mathrm{t}}\cdot\overline{\boldsymbol{F}} = J^{-2/3}\boldsymbol{C} \quad \text{with} \quad \boldsymbol{C} = \boldsymbol{F}^{\mathrm{t}}\cdot\boldsymbol{F}, \tag{3}$$

and four of its invariants, which result from its projection onto the unit tensor $\boldsymbol{I}$, and the undeformed myocardial fiber and sheet unit directions $\boldsymbol{f}_0$ and $\boldsymbol{s}_0$,

$$\begin{aligned} \overline{I}_{\mathrm{I}} &= \overline{\boldsymbol{C}} : \boldsymbol{I} & \overline{I}_{\mathrm{ff}} &= \overline{\boldsymbol{C}} : [\boldsymbol{f}_0\otimes\boldsymbol{f}_0] \\ \overline{I}_{\mathrm{ss}} &= \overline{\boldsymbol{C}} : [\boldsymbol{s}_0\otimes\boldsymbol{s}_0] & \overline{I}_{\mathrm{fs}} &= \overline{\boldsymbol{C}} : [\boldsymbol{f}_0\otimes\boldsymbol{s}_0]. \end{aligned} \tag{4}$$

The invariants $\overline{I}_{\mathrm{ff}}$ and $\overline{I}_{\mathrm{ss}}$ take the interpretation of the isochoric fiber and sheet stretch squared as the squared lengths of the deformed fiber and sheet vectors, $\boldsymbol{f} = \overline{\boldsymbol{F}}\cdot\boldsymbol{f}_0$ and $\boldsymbol{s} = \overline{\boldsymbol{F}}\cdot\boldsymbol{s}_0$, and $\overline{I}_{\mathrm{fs}}$

indicates the fiber-sheet shear. In what follows, we denote the material time derivative as $\{\dot{\circ}\} = \mathrm{d}\{\circ\}/\mathrm{d}t$ and the material gradient and divergence as $\nabla\{\circ\}=\mathrm{d}\{\circ\}/\mathrm{d}\boldsymbol{X}$ and $\mathrm{Div}\,\{\circ\}=\mathrm{d}\{\circ\}/\mathrm{d}\boldsymbol{X}:\boldsymbol{I}$.

2.2. Balance equations

We characterize the electrical problem through the monodomain version of the FitzHugh–Nagumo equations (Fitzhugh, 1961; Nagumo et al., 1962) for the electrical potential ϕ and the mechanical problem through the balance of linear momentum for the deformation $\boldsymbol{\varphi}$,

$$\begin{aligned}\dot{\phi} &= \mathrm{Div}(\boldsymbol{q}) + f^{\phi}\\ 0 &= \mathrm{Div}(\boldsymbol{P}) + \boldsymbol{f}^{\varphi}.\end{aligned} \tag{5}$$

Here, $\boldsymbol{q}$ is the electrical flux, f^{ϕ} is the transmembrane current, $\boldsymbol{P}$ is the Piola stress, and $\boldsymbol{f}^{\varphi}$ is the external mechanical force.

2.3. Constitutive equations

To close the set of equations, we specify the constitutive equations for the electrical flux $\boldsymbol{q}$, the transmembrane current f^{φ}, the Piola stress $\boldsymbol{P}$, and the external mechanical force $\boldsymbol{f}^{\phi}$. We introduce the electrical flux proportional to the gradient of the electrical field,

$$\boldsymbol{q} = \boldsymbol{D}\cdot\nabla\phi, \tag{6}$$

where $\boldsymbol{D}=d^{\mathrm{iso}}\boldsymbol{I} + d^{\mathrm{ani}}\boldsymbol{f}_0\otimes\boldsymbol{f}_0$ denotes the conductivity tensor, which consists of an isotropic contribution d^{iso} and an anisotropic contribution d^{ani} to account for faster conductivity along the fiber direction $\boldsymbol{f}_0$ (Dal et al., 2012). For the transmembrane current,

$$f^{\phi} = c\,\phi[\phi-\alpha][\phi-1] - r\phi, \tag{7}$$

we assume a cubic polynomial, $c\,\varphi\,[\varphi-\alpha][\varphi-1]$, which controls the fast upstroke of the action potential through the parameters c and α (Fitzhugh, 1961; Nagumo et al., 1962), and of a coupling term, which controls the slow repolarization through the recovery variable r (Aliev and Panfilov, 1996). We treat the recovery variable as internal variable, which evolves according to the following equation,

$$\dot{r} = [\gamma + r\,\mu_1/[\mu_2+\phi]][-r - c\,\phi[\phi-\beta-1]], \tag{8}$$

where the recovery parameters γ, μ_1, μ_2 and β control the restitution behavior (Aliev and Panfilov, 1996). We assume that the tissue stress consists of passive and active contributions, $\boldsymbol{P} = \boldsymbol{P}^{\mathrm{pas}} + \boldsymbol{P}^{\mathrm{act}}$, and postulate a Holzapfel-type free energy for the passive tissue stress (Holzapfel and Ogden, 2009), which we further decompose into volumetric and isochoric contributions, $\boldsymbol{P}^{\mathrm{pas}} = \boldsymbol{P}^{\mathrm{vol}} + \boldsymbol{P}^{\mathrm{iso}}$, such that

$$\boldsymbol{P} = \boldsymbol{P}^{\mathrm{vol}} + \boldsymbol{P}^{\mathrm{iso}} + \boldsymbol{P}^{\mathrm{act}} = \boldsymbol{P}^{\mathrm{vol}} + \overline{\boldsymbol{P}} : \mathbb{P} + \boldsymbol{P}^{\mathrm{act}}. \tag{9}$$

$\mathbb{P}$ is the isochoric projection tensor (Holzapfel, 2000), and the volumetric, isochoric, and active stresses take the following forms,

$$\begin{aligned}\boldsymbol{P}^{\mathrm{vol}} &= \kappa\big[J^2-1\big]\boldsymbol{F}^{-\mathrm{t}}\\ \overline{\boldsymbol{P}} &= a\exp\big(b\big[\bar{I}_{\mathrm{I}}-3\big]\big)\overline{\boldsymbol{F}}\\ &= 2a_{\mathrm{ff}}\big[\bar{I}_{\mathrm{ff}}-1\big]\exp\Big(b_{\mathrm{ff}}\big[\bar{I}_{\mathrm{ff}}-1\big]^2\Big)\overline{\boldsymbol{f}}\otimes\boldsymbol{f}_0\\ &\quad +2a_{\mathrm{ss}}\big[\bar{I}_{\mathrm{ss}}-1\big]\exp\Big(b_{\mathrm{ss}}\big[\bar{I}_{\mathrm{ss}}-1\big]^2\Big)\overline{\boldsymbol{s}}\otimes\boldsymbol{s}_0\\ &\quad +a_{\mathrm{fs}}\bar{I}_{\mathrm{fs}}\exp\Big(b_{\mathrm{fs}}\bar{I}_{\mathrm{fs}}^2\Big)\big[\overline{\boldsymbol{f}}\otimes\boldsymbol{s}_0+\overline{\boldsymbol{s}}\otimes\boldsymbol{f}_0\big]\\ \boldsymbol{P}^{\mathrm{act}} &= T^{\mathrm{act}}[\boldsymbol{f}\otimes\boldsymbol{f}_0 + \nu\,\boldsymbol{s}\otimes\boldsymbol{s}_0].\end{aligned} \tag{10}$$

Here, κ is the bulk modulus, a, b, a_{ff}, b_{ff}, a_{ss}, b_{ss}, a_{fs}, b_{fs} are the parameters of the orthotropic Holzapfel model (Göktepe et al., 2011; Holzapfel and Ogden, 2009), and ν_{ff} and ν_{ss} are the weighting factors for active stress generation (Rossi et al., 2012; Walker et al., 2005). The active muscle traction is driven by changes in the electrical potential and obeys the following evolution equation (Göktepe and Kuhl, 2010),

$$\dot{T}^{\mathrm{act}} = \varepsilon(\phi)\big[k_T[\phi-\phi_r] - T^{\mathrm{act}}\big]. \tag{11}$$

The parameters k_T and φ_r control the maximum active force and the resting potential (Nash and Panfilov, 2004). The activation function $\varepsilon = \varepsilon_0 + [\varepsilon_\infty - \varepsilon_0]\exp(-\exp(-\xi[\phi-\overline{\phi}]))$ ensures a smooth activation of the muscle traction T^{act} in terms of the limiting values ε_0 at $\varphi\to-\infty$ and ε_∞ at $\varphi\to+\infty$, the phase shift $\overline{\phi}$, and the transition slope ξ (Göktepe and Kuhl, 2010). In the following, we assume that we can neglect the effects of external forces, $\boldsymbol{f}^{\phi}=\boldsymbol{0}$.

3. Computational model

In this section, we illustrate the finite element discretization of the governing equations, demonstrate their consistent linearization, and discuss the handling of their internal variables (Bonet and Wood, 1997).

3.1. Strong and weak forms

To derive the weak form of the governing equations, we reformulate the electrical and mechanical balance equation (5) in their residual forms and introduce the electrical and mechanical residuals R^{φ} and $\mathbf{R}^{\phi}$ throughout the entire cardiac domain $\mathscr{B}_0$.

$$\begin{aligned}\mathrm{R}^{\phi} &= \dot{\phi} - \mathrm{Div}(\boldsymbol{q}) - f^{\phi} \doteq 0\\ \mathbf{R}^{\varphi} &= -\mathrm{Div}(\boldsymbol{P}) - \boldsymbol{f}^{\varphi} \doteq \boldsymbol{0}.\end{aligned} \tag{12}$$

We prescribe Dirichlet boundary conditions $\phi = \overline{\phi}$ and $\boldsymbol{\varphi} = \overline{\boldsymbol{\varphi}}$ on the Dirichlet boundary and Neumann boundary conditions $\boldsymbol{q}\cdot\boldsymbol{N} = \overline{t}^{\phi}$ and $\boldsymbol{P}\cdot\boldsymbol{N} = \overline{\boldsymbol{t}}^{\varphi}$ on the Neumann boundary with outward normal $\boldsymbol{N}$. For simplicity, we assume that all Neumann boundary conditions are homogeneous, $\overline{t}^{\phi} = 0$ and $\overline{\boldsymbol{t}}^{\varphi} = \boldsymbol{0}$. We multiply the residuals (12) by the scalar- and vector-valued test functions, $\delta\phi$ and $\delta\boldsymbol{\varphi}$, integrate them over the domain $\mathscr{B}_0$, and integrate the flux terms by parts to obtain the weak forms of the electrical and mechanical problems,

$$\begin{aligned}\mathrm{G}^{\phi} &= \int_{\mathcal{B}_0}\delta\phi\dot{\phi}\,\mathrm{d}V + \int_{\mathcal{B}_0}\nabla\delta\phi\cdot\boldsymbol{q}\,\mathrm{d}V - \int_{\mathcal{B}_0}\delta\phi f^{\phi}\,\mathrm{d}V \doteq 0\\ \mathrm{G}^{\varphi} &= \int_{\mathcal{B}_0}\nabla\delta\boldsymbol{\varphi} : \boldsymbol{P}\,\mathrm{d}V - \int_{\mathcal{B}_0}\delta\boldsymbol{\varphi}\cdot\boldsymbol{f}^{\varphi}\,\mathrm{d}V \doteq 0\end{aligned} \tag{13}$$

Next, we discretize the weak forms (13) in time and space.

3.2. Temporal and spatial discretizations

To discretize the weak form of the electrical problem (13.1) in time, we partition the time interval of interest $\mathcal{T}$ into n_{step} discrete subintervals $[t_{\mathrm{n}},t_{\mathrm{n+1}}]$ of length $\Delta t = t_{\mathrm{n+1}} - t_{\mathrm{n}}$,

$$\mathcal{T} = \mathbf{U}_{\mathrm{n}=1}^{n_{\mathrm{step}}}[t_{\mathrm{n}}, t_{\mathrm{n+1}}], \tag{14}$$

and adopt a finite difference discretization in combination with a classical implicit Euler backward scheme to determine the electrical potential φ at the current time point $t_{\mathrm{n+1}}$,

$$\dot{\phi} = [\phi - \phi_{\mathrm{n}}]/\Delta t. \tag{15}$$

To discretize the weak forms of the electrical and mechanical problems (13.1) and (13.2) in space, we partition the domain of interest $\mathcal{B}_0$ into n_{el} discrete subdomains $\mathcal{B}_0^{\mathrm{e}}$,

$$\mathcal{B}_0 = \mathbf{U}_{e=1}^{n_{el}} \mathcal{B}_0^e \tag{16}$$

and adopt a finite element discretization in combination with a classical Bubnov-Galerkin scheme to discretize the test functions $\delta\phi$ and $\delta\boldsymbol{\varphi}$ and trial functions ϕ and $\boldsymbol{\varphi}$ in space (Göktepe and Kuhl, 2010),

$$\begin{aligned} \delta\phi &= \sum_{i=1} N_i \delta\phi_i \quad \delta\boldsymbol{\varphi} = \sum_{j=1} N_j \delta\boldsymbol{\varphi}_j \\ \phi &= \sum_{k=1} N_k \phi_k \quad \boldsymbol{\varphi} = \sum_{l=1} N_l \boldsymbol{\varphi}_l. \end{aligned} \tag{17}$$

Here, N are the standard isoparametric shape functions.

3.3. Residuals and consistent linearization

With the discretizations in time (15) and space (17), we can reformulate the weak forms (13) as the discrete algorithmic residuals of the electrical and mechanical problems,

$$\begin{aligned} \mathrm{R}_I^{\phi} &= \mathbf{A}_{e=1}^{n_{el}} \int_{\mathcal{B}_0^e} N_i \frac{\phi - \phi_n}{\Delta t} + \nabla N_i \cdot \boldsymbol{q} - N_i f^{\phi} \mathrm{d}V_e \doteq 0 \\ \mathbf{R}_J^{\varphi} &= \mathbf{A}_{e=1}^{n_{el}} \int_{\mathcal{B}_0^e} \nabla N_j \cdot \boldsymbol{P} - N_j \boldsymbol{f}^{\varphi} \mathrm{d}V_e \doteq \mathbf{0} \end{aligned} \tag{18}$$

The operator $\mathbf{A}$ symbolizes the assembly of all element residuals at the element nodes i and j to the global residuals at the global nodes I and J. To solve for the unknown nodal electrical potential ϕ_I and mechanical deformation $\boldsymbol{\varphi}_J$, we could, for example, adapt an incremental interactive Newton–Raphson solution strategy based on the consistent linearization of the governing equations,

$$\begin{aligned} \mathrm{R}_I^{\phi} + \sum_K \mathrm{K}_{IK}^{\phi\phi} \mathrm{d}\phi_K + \sum_L \mathbf{K}_{IL}^{\phi\varphi} \cdot \mathrm{d}\boldsymbol{\varphi}_L \doteq 0 \\ \mathbf{R}_J^{\varphi} + \sum_K \mathbf{K}_{JK}^{\varphi\phi} \mathrm{d}\phi_K + \sum_L \mathbf{K}_{JL}^{\varphi\varphi} \cdot \mathrm{d}\boldsymbol{\varphi}_L \doteq 0. \end{aligned} \tag{19}$$

The solution of this system of equation (19) with the discrete residuals (18) and the iteration matrices,

$$\begin{aligned} \mathrm{K}_{IK}^{\phi\phi} &= \mathbf{A}_{e=1}^{n_{el}} \int_{\mathcal{B}_0^e} N_i \left[\frac{1}{\Delta t} - \mathrm{d}_{\phi} f^{\phi} \right] N_k + \nabla N_i \cdot \boldsymbol{D} \cdot \nabla N_k \mathrm{d}V_e \\ \mathbf{K}_{IL}^{\phi\varphi} &= \mathbf{A}_{e=1}^{n_{el}} \int_{\mathcal{B}_0^e} \nabla N_i \cdot \mathrm{d}_{\boldsymbol{F}} \boldsymbol{q} \cdot \nabla N_l \mathrm{d}V_e \\ \mathbf{K}_{JK}^{\varphi\phi} &= \mathbf{A}_{e=1}^{n_{el}} \int_{\mathcal{B}_0^e} \nabla N_j \cdot \mathrm{d}_{\phi} \boldsymbol{P}^{\mathrm{act}} N_k \mathrm{d}V_e \\ \mathbf{K}_{JL}^{\varphi\varphi} &= \mathbf{A}_{e=1}^{n_{el}} \int_{\mathcal{B}_0^e} \nabla N_j \cdot \mathrm{d}_{\boldsymbol{F}} \boldsymbol{P} \cdot \nabla N_l \mathrm{d}V_e, \end{aligned} \tag{20}$$

defines the iterative update of the global vector of electrical and mechanical unknowns $\phi_I \leftarrow \phi_I + \mathrm{d}\phi_I$ and $\boldsymbol{\varphi}_J \leftarrow \boldsymbol{\varphi}_J + \mathrm{d}\boldsymbol{\varphi}_J$. It remains to specify the fluxes $\boldsymbol{q}$ and $\boldsymbol{P}$ and sources f^{ϕ} and $\boldsymbol{f}^{\varphi}$ for the residuals (18.1) and (18.2) and their sensitivities with respect to the primary unknowns ϕ and $\boldsymbol{\varphi}$ for the iteration matrices (20.1) to (20.4) (Dal et al., 2013; Göktepe and Kuhl, 2010).

3.4. Internal variables

To integrate the evolution equations of the recovery variable r and the active muscle traction T^{act} in time, we treat both as internal variables and update and store them locally on the integration point level (Göktepe and Kuhl, 2010; Krishnamoorthi et al., 2013). To solve the nonlinear evolution equation (8) for the recovery variable r, we locally adopt a finite difference discretization in combination with a classical implicit Euler backward scheme (Göktepe and Kuhl, 2009),

$$\dot{r} = [r - r_k]/\Delta t, \tag{21}$$

and introduce the local residual R^r,

$$\mathrm{R}^r = r - r_k - \gamma \Delta t + \frac{\mu_1 r}{\mu_2 + \phi} [r + c\,\phi[\phi - \beta - 1]] \Delta t = 0, \tag{22}$$

and its algorithmic linearization K^r,

$$\mathrm{K}^r = 1 + \frac{\mu_1}{\mu_2 + \phi} [2r - c\,\phi[\phi - \beta - 1]] \Delta t. \tag{23}$$

to iteratively update the recovery variable as $r \leftarrow r - \mathrm{R}^r / \mathrm{K}^r$ (Kotikanyadanam et al., 2010). To solve the linear evolution equation (11) for the active muscle traction T^{act}, we again adopt a finite difference discretization in time together with an implicit Euler backward scheme,

$$\dot{T}^{\mathrm{act}} = [T^{\mathrm{act}} - T_k^{\mathrm{act}}]/\Delta t \tag{24}$$

and solve the resulting equation directly to calculate the active muscle traction at the current point in time,

$$T^{\mathrm{act}} = [T_k^{\mathrm{act}} + \varepsilon\, k_T [\phi - \phi_r] \Delta t] / [1 + \varepsilon \Delta t], \tag{25}$$

where the $\varepsilon = \varepsilon_0 + [\varepsilon_\infty - \varepsilon_0] \exp(-\exp(-\xi[\phi - \overline{\phi}]))$ (Dal et al., 2013). Once we have determined the recovery variable r and the active muscle traction T^{act}, we calculate the electrical flux $\boldsymbol{q}$ from equation (6), the electrical source f^{φ} from equation (7), the active stress $\boldsymbol{P}^{\mathrm{act}}$ from equation (10), and the total stress $\boldsymbol{P}$ from equation (9) to evaluate the electrical and mechanical residuals (18). Last, we calculate the sensitivities $\mathrm{d}_{\phi} f^{\varphi}$ (Kotikanyadanam et al., 2010), $\mathrm{d}_{\boldsymbol{F}}\, \boldsymbol{q} = \mathbf{0}$, $\mathrm{d}_{\phi} \boldsymbol{P}^{\mathrm{act}} = \partial_{\phi} T^{\mathrm{act}} [\nu_{\mathrm{ff}}\, \boldsymbol{f} \otimes \boldsymbol{f}_0 + \nu_{\mathrm{ss}}\, \boldsymbol{s} \otimes \boldsymbol{s}_0]$, and $\mathrm{d}_{\boldsymbol{F}} \boldsymbol{P}$ (Göktepe et al., 2011) for the electrical and mechanical iteration matrices (20).

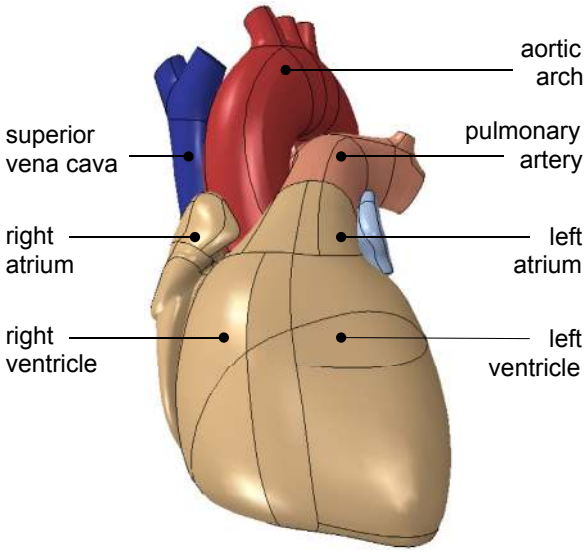

Fig. 3. Solid model of the human heart with anatomic details including the aortic arch, pulmonary artery and superior vena cava, left and right atria, and left and right ventricles.

4. Human heart model

In this section, we illustrate the creation of a solid model, a finite element model, and a muscle fiber model from the anatomic model in Fig. 1 and the creation of a fluid model from the circulatory model in Fig. 2. This work was performed as part of the Living Heart Project.

4.1. Solid model

Fig. 3 shows the solid model of a human heart with well-defined anatomic details including the aortic arch, the pulmonary artery and superior vena cava, the left and right atria, and the left and right ventricles. We adapt the underlying geometry from the three-dimensional computer-aided design model in Fig. 1 (Zygote Media Group and Inc., 2013). The model accurately defines the key features for our finite element analysis including detailed chamber volumes and wall thicknesses.

Fig. 4 illustrates the finite element model of the heart discretized with 208,561 linear tetrahedral elements and 47,323 nodes. This discretization introduces 47,323 electrical degrees of freedom for the scalar-valued potential ϕ and 141,969 mechanical degrees of freedom for the vector-valued deformation $\boldsymbol{\varphi}$ resulting in 189,292 degrees of freedom in total.

Fig. 5 illustrates the corresponding muscle fiber model with 208,561 discrete fiber and sheet directions $\boldsymbol{f}_0$ and $\boldsymbol{s}_0$. The muscle fibers wrap helically around the heart. At the epicardium, the outer wall, muscle fibers point clockwise-upwards whereas at the endocardium, the inner wall, they point clockwise-downward. We interpolate the fiber and sheet directions from generic fiber orientation illustrations and assign their discrete values to each integration point of the finite element model (Wong and Kuhl, 2014).

4.2. Fluid model

Fig. 6 illustrates the blood flow model with a surface-based fluid cavity representation of the four chambers, the right atrium, the right ventricle, the left atrium, and the left ventricle (Abaqus 6.13. Analysis Use, 2013). These chambers are connected through five viscous resistance models of Windkessel type (Berberoglu et al., 2014) representing the tricuspid valve, the pulmonary circulation, the mitral valve, the aortic valve, and the systemic circulation (Smith, 2004). We adapt the positions of these valves and the corresponding chamber volumes from the detailed circulatory model in Fig. 2 (Zygote Media Group and Inc., 2013). We neglect inertia effects and assume that the flow rate between two neighboring chambers, $q_{c \to c+1}$, is proportional to the pressure difference in the two chambers, $p_c - p_{c+1}$, scaled by the resistance $R_{c \to c+1}$ (Frank, 1899),

$$q_{c \to c+1} = \frac{p_c - p_{c+1}}{R_{c \to c+1}}.$$

To represent the four chambers, we create fluid cavities from cubes of unit volume and add the corresponding volume V_c (Abaqus 6.13. Analysis Use, 2013) §11.5. We then define the change in chamber volume,

$$\dot{V}_c = q_{c-1 \to c} - q_{c \to c+1},$$

as the difference between influx $q_{c-1 \to c}$ and outflux $q_{c \to c+1}$ of the corresponding chamber. This simplified approach provides a natural coupling between the structural deformation and the fluid pressure, in which the fluid is represented exclusively in terms of the temporally varying blood pressure in the four chambers. Spatial pressure variations or shear stresses cannot be modeled with this fluid cavity representation.

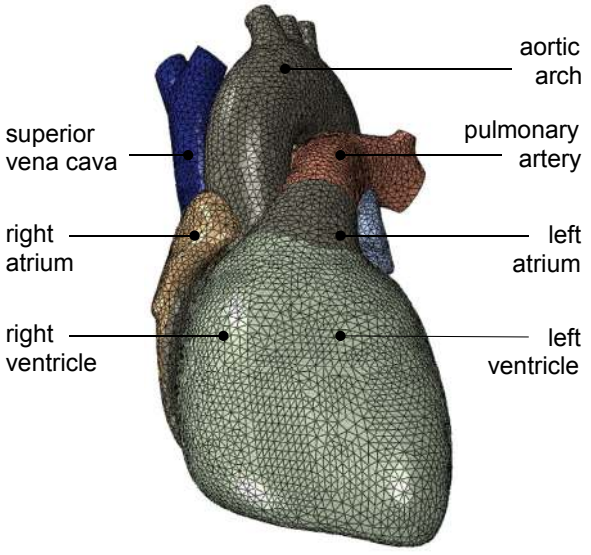

Fig. 4. Finite element model of the human heart discretized with 208,561 linear tetrahedral elements, 47,323 nodes, and 189,292 degrees of freedom, of which 47,323 are electrical and 141,969 are mechanical.

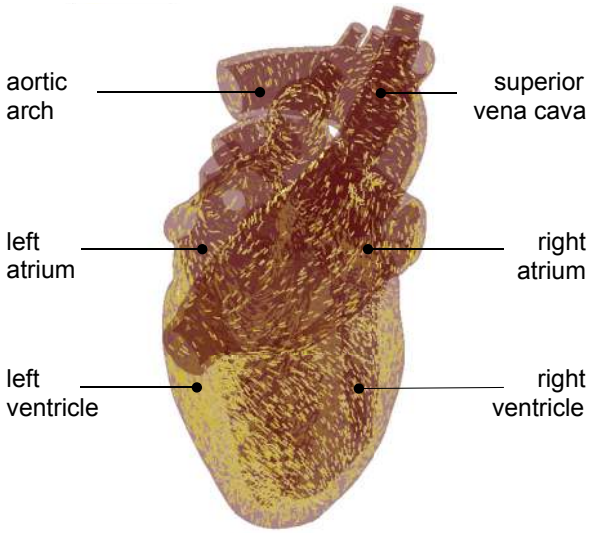

Fig. 5. Muscle fiber model of the human heart with 208,561 discrete fiber and sheet directions interpolated and assigned to each integration point.

4.3. Solid and fluid model parameters

Table 1 summarizes the electrical, mechanical, electromechanical, and flow parameters of the human heart simulation.

For the electrical problem, we choose the initial conditions to φ=−80 mV throughout the entire heart, except for a short excitation phase, during which we locally increase the voltage beyond the excitation threshold in the region of the sinoatrial node located between the right atrium and the superior vena cava. For the mechanical problem, we adopt a combination of different boundary conditions. At the epicardium, the outer wall, we fix the heart in space through connector elements with a moderate elastic stiffness

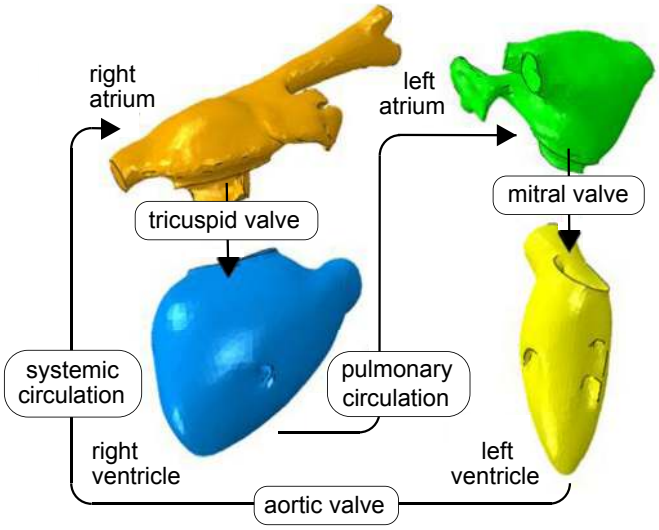

Fig. 6. Blood flow model of the human heart with surface-based fluid cavity representation of the right atrium, right ventricle, left atrium, and left ventricle connected through viscous resistance models of Windkessel type for the tricuspid valve, pulmonary circulation, mitral valve, aortic valve, and systemic circulation.

situated at the intersection between the four-chamber heart and its vasculature (Abaqus 6.13. Analysis Use, 2013) §31.2, similar to supporting the heart by linear elastic springs (Göktepe and Kuhl, 2010). At the endocardium, the inner wall, we control the pressure-volume relation through surface-based fluid cavities (Abaqus 6.13. Analysis Use, 2013) §11.5. We choose the initial conditions according to a preload step, during which we pressurize the right atrium and ventricle with 0.266 kPa and the left atrium and ventricle with 0.533 kPa.

5. Results

To demonstrate the ability of the proposed model to accurately represent the basic features of cardiac excitation and contraction, we simulate the electro-mechanical response of the human heart throughout a representative cardiac cycle.

Table 1
Model parameters of the human heart simulation.

Electrical			
Conduction	$d^{\text{iso}} = 2$ mm^2/ms	$d^{\text{ani}} = 6$ mm^2/ms	(Göktepe and Kuhl, 2010)
Excitation	$\alpha = 0.01$	$\gamma = 0.002$	(Göktepe et al., 2010)
	$\beta = 0.15$	$c = 8$	(Kotikanyadanam et al., 2010)
	$\mu_1 = 0.2$	$\mu_2 = 0.3$	(Aliev and Panfilov, 1996)
Mechanical			
Passive	$\kappa = 1{,}000$ kPa		
	$a = 0.496$ kPa	$b = 7.209$	(Göktepe et al., 2011)
	$a_{\text{ff}} = 15.193$ kPa	$b_{\text{ff}} = 20.417$	(Göktepe et al., 2011)
	$a_{\text{ss}} = 3.283$ kPa	$b_{\text{ss}} = 11.176$	(Göktepe et al., 2011)
	$a_{\text{fs}} = 0.662$ kPa	$b_{\text{fs}} = 9.466$	(Göktepe et al., 2011)
Active	$\nu_{\text{ff}} = 1.0$	$\nu_{\text{ss}} = 0.4$	(Walker et al., 2005)
	$k_T = 0.49$ kPa/mV	$\varphi_r = -80$ mV	(Dal et al., 2013)
Coupling			
Activation	$\varepsilon_0 = 0.1$/mV	$\varepsilon_\infty = 1.0$/mV	(Göktepe and Kuhl, 2010)
	$\xi = 1$/mV	$\bar{\phi} = 0$ mV	(Göktepe and Kuhl, 2010)
Blood flow			
Blood	$\rho = 1.025 \cdot 10^{-6}$ kg/mm^3		(Shmukler, 2004)
Valves	$R^{\text{tv}} = 0.0010$ kPa ms/mm^3		(Smith, 2004)
	$R^{\text{mv}} = 0.0061$ kPa ms/mm^3		(Smith, 2004)
	$R^{\text{av}} = 0.0027$ kPa ms/mm^3		(Smith, 2004)
Circulation	$R^{\text{pc}} = 0.0104$ kPa ms/mm^3		
	$R^{\text{sc}} = 0.0850$ kPa ms/mm^3		

5.1. Electrical and mechanical fields

Fig. 7 displays the spatio-temporal evolution of the electrical potential, ϕ, the mechanical displacement, $\boldsymbol{u} = \| \boldsymbol{\varphi} - \boldsymbol{X} \|$, and the muscle fiber strain, $E_{\text{ff}} = \boldsymbol{E}:[\boldsymbol{f}_0 \otimes \boldsymbol{f}_0]$, across the human heart. The displacement u illustrates the magnitude of the displacement vector $\boldsymbol{u}$ as the difference between the current position $\boldsymbol{\varphi}$ and initial position $\boldsymbol{X}$. The muscle fiber strain E_{ff} indicates the strain along the muscle fiber direction $\boldsymbol{f}_0$. Initially the heart is at rest and its cells are negatively charged with a potential of $\phi = -80$ mV, see Fig. 7, top row. The heart is excited from the sinoatrial node, a region between the right atrium and the superior vena cava, which is the first region to depolarize with a potential of $\phi = +20$ mV. The excitation wave spreads rapidly across the atria, arrests briefly at the atrial-ventricular node, and continues to travel along the septum to rapidly excite the left and right ventricles. After a short period of complete depolarization, repolarization spreads gradually across the left and right ventricles and atria to bring the heart back to its unexcited baseline state.

The mechanical deformation clearly follows the electrical signal and spreads from the region that is excited first, the sinoatrial node, across the entire heart, see Fig. 7, middle row. Once the heart is fully excited, the electrical potential is homogeneous across the heart; yet the mechanical deformation is not. This clearly indicates the importance of the spatially varying fiber orientation, which causes a local interplay between cellular contraction and secondary effects induced by neighboring heart muscle fibers. As the electrical potential returns to its baseline state, the deformation gradually decays, the heart relaxes, and prepares for the next filling phase.

The muscle fiber strain mimics the effects of the overall deformation, projected onto the local fiber direction, see Fig. 7, bottom row. During systole, the muscle fibers contract rapidly and shorted up to 20% to induce ventricular ejection. This moves the apex upward toward the base and induces a twist along the heart's long axis. During diastole, the muscle fibers gradually relax to allow for ventricular filling and the apex gradually returns to its initial position.

5.2. Electrical potential throughout a cardiac cycle

Fig. 8 illustrates the local temporal evolution of the electrical potential ϕ for an individual cardiac muscle cell. During excitation, the cell depolarizes rapidly and its electrical potential increases from -80 mV to $+20$ mV within the order of milliseconds. This excitation causes the cell to contract. Unlike nerve cells, cardiac cells briefly plateau at the excited state before they begin to relax. During relaxation, cardiac cells gradually repolarize and return to their stable baseline state at -80 mV.

5.3. Mechanical deformation throughout a cardiac cycle

Fig. 9 illustrates the dynamics of the heart's long axis. During ventricular ejection, the distance between apex and base decreases rapidly and the ventricles shorten by approximately 7 mm. Shortening plateaus towards end systole to ensure that enough blood is ejected. During ventricular filling, the long axis gradually returns to its initial length as the heart muscle relaxes.

Fig. 10 illustrates the pressure-volume loop of the human heart, the temporal evolution of the left ventricular pressure and volume throughout a cardiac cycle. The first phase, ventricular filling, begins with the opening of the mitral valve and continues towards end diastole, the point of maximum volume and minimum pressure in the bottom right corner. The second phase, isovolumetric contraction, is characterized through a steep increase in pressure while the ventricular volume remains unchanged. Once the

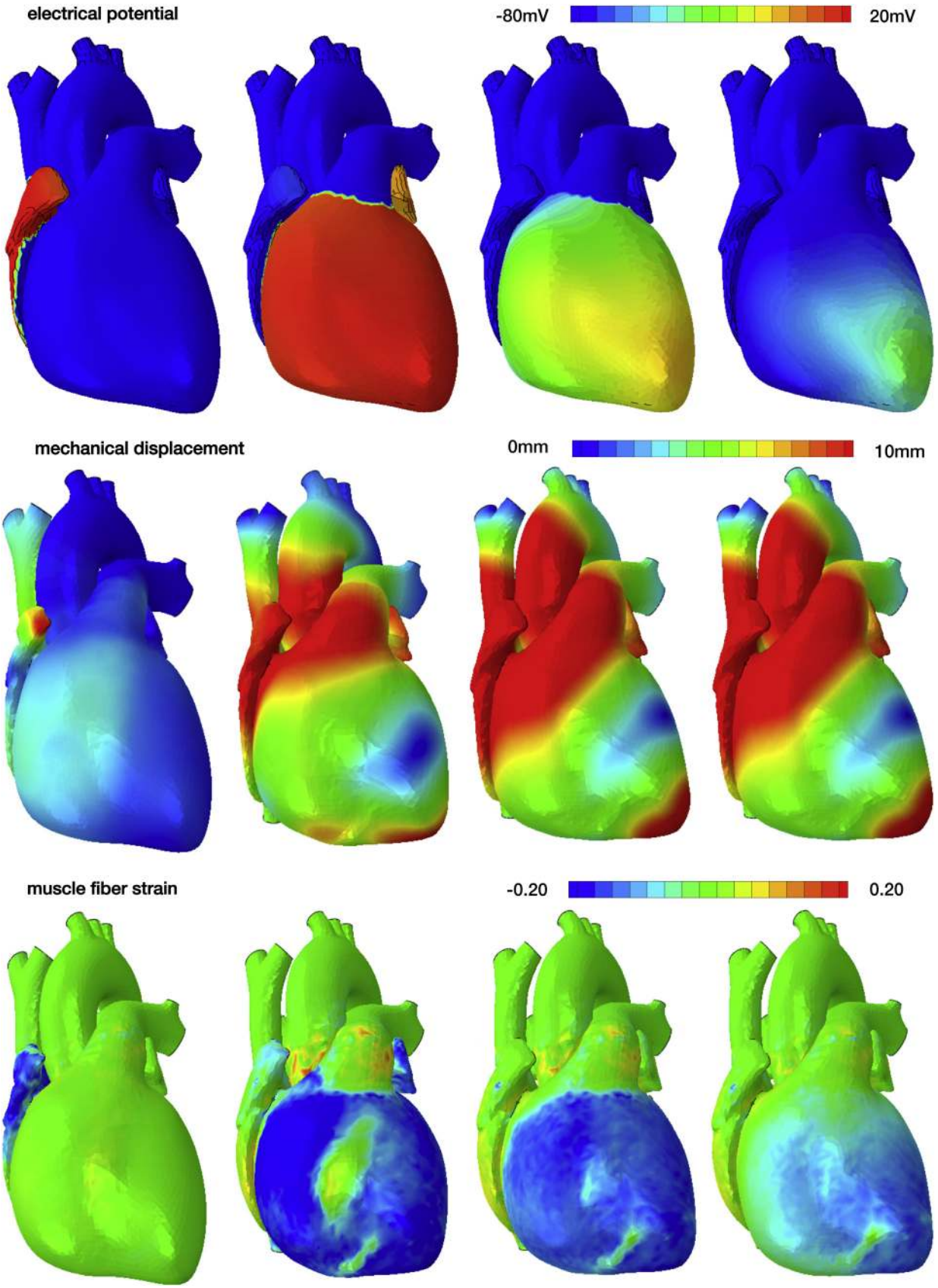

Fig. 7. Spatio-temporal evolution of electrical potential, mechanical displacement, and muscle fiber strain across the human heart. During systole, the heart depolarizes rapidly from −80 mV to +20 mV, the muscle fibers contract and shorten up to 20% to induce ventricular ejection. During diastole, the heart repolarizes gradually from +20 mV to −80 mV, the muscle fibers relax and relengthen to their initial length to induce ventricular filling.

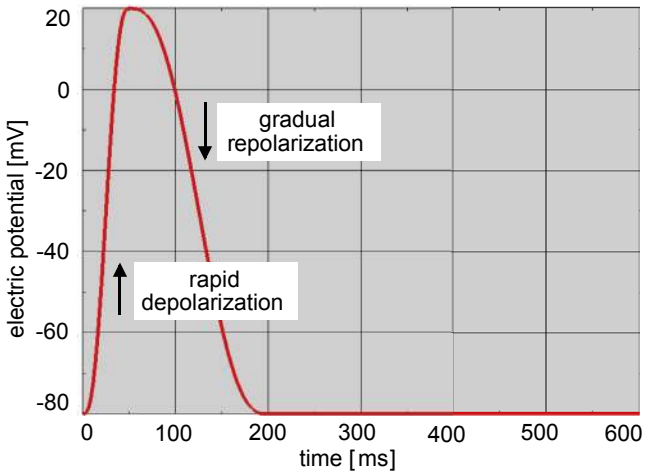

Fig. 8. Temporal evolution of electrical potential. During excitation, cardiac cells rapidly depolarize and the electrical potential increases from −80 mV to +20 mV within the order of milliseconds. During relaxation, cardiac cells gradually repolarize and return to the stable baseline state at −80 mV.

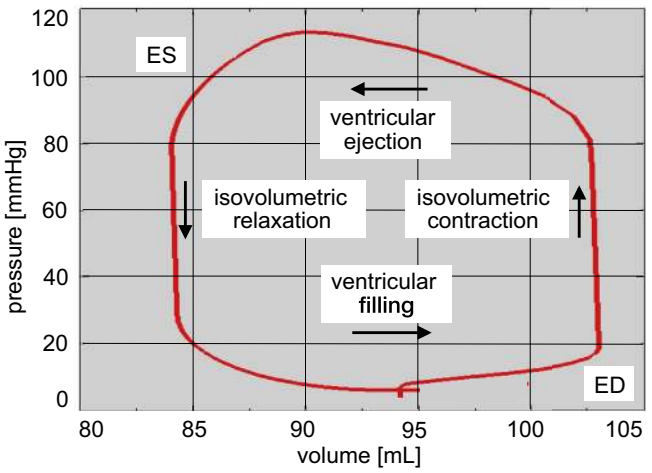

Fig. 10. Pressure-volume loop of the human heart with characteristic phases of ventricular filling, isovolumetric contraction, ventricular ejection, and isovolumetric relaxation. The enclosed area characterizes the work performed throughout the cardiac cycle.

ventricular pressure exceeds the aortic pressure the aortic valve opens. This is the beginning of the third phase, ventricular ejection, during which the volume of the ventricle decreases, while the pressure still remains high. Ejection continues towards end systole, the point of minimum volume and maximum pressure in the top left corner. The fourth phase, isovolumetric relaxation, begins with closure of the aortic valve followed by a drastic pressure drop. A new cycle starts with the reopening of the mitral valve and the beginning of ventricular filling.

6. Discussion

Modeling the human heart with all four chambers and all four valves is increasingly recognized as a critical step towards reliable, predictive modeling of cardiac function (Trayanova, 2011). Although the origin of cardiac disease is often strictly local, the consequences are typically spatially and temporally complex, and almost always affect the entire heart (Kumar et al., 2005). Until recently, whole heart simulations were virtually impossible because of a lack of sufficient image resolution and computational power. Recent advances in non-invasive imaging and computer simulation now allows us to create fully three-dimensional models of the entire human heart to explore the interplay between electrical and mechanical fields under healthy, diseased, and treatment conditions (Gonzales et al., 2013). With these goals in mind, we have designed a basic prototype model for excitation–contraction coupling in the human heart.

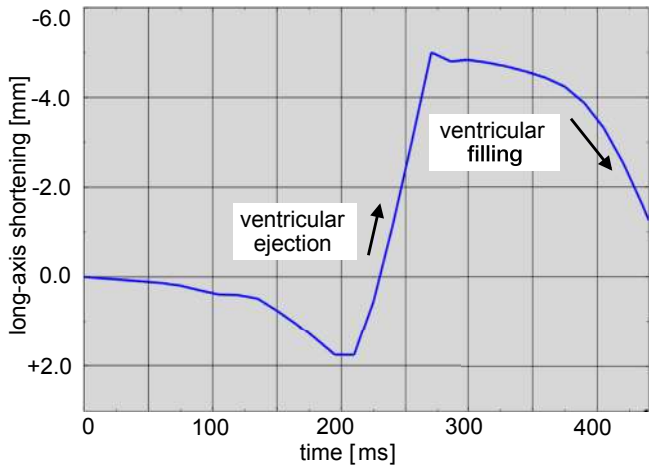

Fig. 9. Temporal evolution of long-axis shortening. During ventricular ejection, the distance between apex and base decreases rapidly as the ventricles shorten by approximately 7 mm. During ventricular filling, the long axis gradually returns to its initial length as the heart muscle relaxes.

In this proof-of-concept study, we have demonstrated that it is feasible to model whole heart function within a single, unified finite-element based modeling environment. First, we have shown that our whole heart simulation predicts spatio-temporal profiles of the electrical potential, the mechanical deformation, and the muscle fiber strain, which agree nicely with clinical observations and engineering intuition (Wong et al., 2013). Throughout the cardiac cycle, the electrical potential varies between −80 mV and +20 mV, the mechanical deformation takes values in the 10 mm regime, and the maximum muscle fiber contraction is in the order of 20%, see Fig. 7. Second, we have illustrated how our heart muscle cells locally depolarize rapidly from the resting state at −80 mV to the excited state at +20 mV and depolarize gradually from +20 mV back to −80 mV (Göktepe and Kuhl, 2009), see Fig. 8. Last, we have globally extracted metrics of cardiac function, long-axis shortening and pressure-volume loops, see Figs. 9 and 10. Our long-axis shortening of approximately 7.0 mm agrees nicely with previous simulations of a bi-ventricular human heart model, which predicted a shortening of 7.6 mm (Wong et al., 2013) and with clinical observations (Robers et al., 1991). Our pressure-volume loop with left ventricular volumes between 83 mL and 103 mL and pressures between 5 mmHg and 118 mmHg lies nicely within the clinically expected range (Berberoglu et al., 2014; Burghoff, 2013). Our current run time for the electro-mechanical simulation of an entire cardiac cycle is 94 minutes on a standard 16 CPU machine.

6.1. Limitations and future perspectives

Our geometric representation of the human heart is promising and our first simulations are encouraging, both from an engineering and clinical perspective. Yet, our current model has a few limitations, which can be addressed with modular changes and refinements. In particular, our ongoing work aims to implement the following enhancements:

For the electrical module, as a first step, we have assumed that the cellular response is homogeneous across the heart. Recent studies have shown that cellular heterogeneity is critical to accurately represent the electrical activation sequence of the heart: The first regions to depolarize are the last to repolarize (Keener and Sneyd, 2004). This is true for both regional and transmural activation and can be addressed via different cell types or via a spatially varying refractoriness (Hurtado and Kuhl, 2014). In addition, cellular conduction varies hugely between standard cardiac muscle cells and Purkinje fiber cells, which are fast-conducting cells that transmit the electrical signal rapidly from the atrioventricular node to the apex (Keener and Sneyd, 2004). We can incorporate this fast conduction, which is critical for bottom up excitation, by adding one-dimensional cable elements across the inner wall (Kotikanyadanam et al., 2010).

For the mechanical module, probably the most significant limitation is the parameter identification, which has been performed on explanted tissue samples. Recent studies have indicated that in vivo properties can be up to four orders of magnitude different from ex vivo properties (Rausch and Kuhl, 2013). Ideally, a series of in vivo experiments should be designed around calibrating these parameters in the beating heart (Tsamis et al., 2011). While the passive properties are relatively easy to access, identifying the active properties can be challenging. Here we have assumed a phenomenological representation of active contraction through equations (10) and (11). Integrating cellular phenomena such as calcium release, actin-myosin sliding, and cross bridging could provide a more mechanistic representation of active force generation (Murtada et al., 2012). The current trend is to replace active stress with active strain (Göktepe et al., 2014; Pezzuto et al., 2014), a property that is easier to interpret, easier to bound with physically meaningful values, easier to link to tissue microstructure (Rossi et al., 2014), and easier to measure overall.

For the interaction between the electrical and mechanical fields, we have assumed that coupling is primarily uni-directional: Changes in the electrical field ϕ induce major changes in the mechanical field $\boldsymbol{\varphi}$, while changes in the mechanical field only induce marginal or no changes in the electrical field. The entries of the coupling matrices $\mathbf{K}_{JK}^{\varphi\phi}$ and $\mathbf{K}_{IL}^{\phi\varphi}$ and in equations (20.2) and (20.3) provide quantitative insight into the nature of these coupling effects, which manifest themselves in the active stress $\boldsymbol{P}^{\text{act}}$, the electrical flux $\boldsymbol{q}$, and the electrical source f^{phi}. Our current model neglects the effects of mechanical deformation on the electrical field (Göktepe and Kuhl, 2010). These phenomena, which are commonly believed to be of minor importance, come in two flavors: A mechanically sensitive flux $\boldsymbol{q}(\boldsymbol{F})$ would mimic stretch-induced changes in conductivity, whereas a mechanically sensitive source $f^{\phi}(\boldsymbol{F})$ would mimic the effect of stretch-activated ion channels (Markhasin et al., 2003). Neglecting these effects allows us to solve the electrical and mechanical problems in a decoupled way. While we ultimately aim to solve the coupled problem of electro-mechanics in equation (19) fully monolithically, here, we solve the electrical module (19.1) using Abaqus/Standard 6.13 and the mechanical module (19.2) using Abaqus/Explicit 6.13 (Abaqus 6.13. Analysis Use, 2013).

For the fluid module, we have assumed a simplified resistance model of Windkessel type (Frank, 1899). While some approaches suggest to improve this model with additional capacitors or time-varying resistances (Smith, 2004), our ultimate goal is to replace the compartment approach with a real fluid simulation. A fully coupled fluid–structure interaction model of the human heart is highly desirable, albeit hugely challenging, and the major research thrust in numerous groups around the world. Including fluid flow would allow us to predict shear stresses on the myocardial wall, and more importantly, on the four heart valves, throughout the entire cardiac cycle (de Hart et al., 2003). This presents tremendous opportunities to better understand the mechanisms of valvular disease and optimize their treatment in the form of valve repair or replacement, either through open heart surgery or minimally invasive intervention (Gessat et al., 2014).

6.2. Concluding remarks

We have presented a proof-of-concept simulator for cardiac excitation and contraction in the human heart. Using human computer tomography and magnetic resonance images, we have created a whole heart model with all four chambers, connected through four valves. The coordinated opening and closing of these valves regulates the filling of the chambers; the controlled interplay of electrical and mechanical fields coordinates their ejection. To simulate the blood flow from chamber to chamber, we have adopted a classical resistance-based Windkessel model. To simulate passive filling and active contraction, we have implemented a two-field finite element formulation based on coupled electrical and mechanical fields. We have shown that our model is capable of predicting the spatio-temporal evolution of electrical potentials and mechanical deformation across the heart. From these, we have extracted two common metrics of cardiac function, long-axis shortening and pressure-volume loops, which agreed well with clinical observations. Our ultimate goal is to employ our human heart simulator to probe landscapes of clinical parameters, and guide device design and treatment planning in cardiac diseases of the aortic, pulmonary, tricuspid, or mitral valve such as stenosis, regurgitation, or prolapse, and in other forms of cardiac dysfunction.

Acknowledgments

This work was performed as part of the Living Heart Project. The authors thank Dr. Julius M. Guccione, Dr. Manuel K. Rausch, Dr. Jonathan Wong, and Dr. Martin Genet for stimulating discussions. Ellen Kuhl acknowledges support by the National Science Foundation CAREER award CMMI 0952021, by the National Science Foundation INSPIRE grant 1233054, and by the National Institutes of Health grant U54 GM072970.

References

Abaqus 6.13. Analysis User's Manual, 2014. Simulia. Dassault Systèmes.
American Heart Association, 2014. Heart disease and stroke statistics 2014 update. Circulation 129, e28–e292.
Aliev, R.R., Panfilov, A.V., 1996. A simple two-variable model of cardiac excitation. Chaos 7, 293–301.
Berberoglu, E., Solmaz, H.O., Göktepe, S., 2014. Computational modeling of coupled cardiac electromechanics incorporating cardiac dysfunctions. Euro. J. Mech. A/Solids 48, 60–73 .
Berne, R.M., Levy, M.N., 2001. Cardiovascular Physiology. In: The Mosby Monograph Series.
Bonet, J., Wood, R.D., 1997. Nonlinear Continuum Mechanics for Finite Element Analysis. Cambridge University Press.
Braunwald, E., 1997. Heart Disease: A Textbook of Cardiovascular Medicine. W.B. Saunders Company.
Burghoff, D., 2013. Pressure-volume loops in clinical research. J. Am. Coll. Cardiol. 62, 1173–1176.
Dal, H., Göktepe, S., Kaliske, M., Kuhl, E., 2012. A fully implicit finite element method for bidomain models of cardiac electrophysiology. Comp. Meth. Biomech. Biomed. Eng. 15, 645–656.
Dal, H., Göktepe, S., Kaliske, M., Kuhl, E., 2013. A fully implicit finite element method for bidomain models of cardiac electromechanics. Comp. Meth. Appl. Mech. Eng. 253, 323–336.
Eriksson, T.S.E., Prassl, A.J., Plank, G., Holzapfel, G.A., 2013. Modeling the dispersion in electromechanically coupled myocardium. Int. J. Num. Meth. Biomed. Eng. 29, 1267–1284.
Fitzhugh, R., 1961. Impulses and physiological states in theoretical models of nerve induction. Biophys. J. 1, 455–466.
Frank, O., 1899. Die Grundform des arteriellen Pulses. Ztg. für Biol. 37, 483–586.

Gessat, M., Hopf, R., Pollok, T., Russ, C., Frauenfelder, T., Sundermann, S.H., Hirsch, S., Mazza, E., Szekely, G., Falk, V., 2014. Image-based mechanical analysis of stent deformation: concept and exemplary implementation for aortic valve stents. IEEE Trans. Biomed. Eng. 61, 4–15.

Göktepe, S., Kuhl, E., 2009. Computational modeling of electrophysiology: a novel finite element approach. Int. J. Num. Meth. Eng. 79, 156–178.

Göktepe, S., Kuhl, E., 2010. Electromechanics of the heart – a unified approach to the strongly coupled excitation–contraction problem. Comp. Mech. 45, 227–243.

Göktepe, S., Wong, J., Kuhl, E., 2010. Atrial and ventricular fibrillation – computational simulation of spiral waves in cardiac tissue. Arch. Appl. Mech. 80, 569–580.

Göktepe, S., Acharya, S.N.S., Wong, J., Kuhl, E., 2011. Computational modeling of passive myocardium. Int. J. Num. Meth. Biomed. Eng. 27, 1–12.

Göktepe, S., Menzel, A., Kuhl, E., 2014. The Generalized Hill Model: a Kinematic Approach Towards Active Muscle Contraction. J. Mech. Phys. Solids..

Gonzales, M.J., Sturgeon, G., Krishnamurthy, A., Hake, J., Jonas, R., Stark, P., Rappel, W.J., Narayan, S.M., Zhang, Y., Segars, W.P., McCulloch, A.D., 2013. A three-dimensional finite element model of human arterial anatomy: new methods for cubic Hermite meshes with extraordinary ventricles. Med. Im. Anal. 17, 525–537.

de Hart, J., Peters, G.W.M., Schreurs, P.J.G., Baaijens, F.P.T., 2003. A three-dimensional computational analysis of fluid-structure interaction in the aortic valve. J. Biomech. 36, 103–112.

Holzapfel, G.A., 2000. Nonlinear Solid Mechanics: a Continuum Approach for Engineering. John Wiley & Sons.

Holzapfel, G.A., Ogden, R.W., 2009. Constitutive modelling of passive myocardium: a structurally based framework for material characterization. Phil. Trans. A 367, 3445–3475.

Hunter, P.J., Pullan, A.J., Smaill, B.H., 2003. Modeling total heart function. Ann. Rev. Biomed. Eng. 5, 147–177.

Hurtado, D.E., Kuhl, E., 2014. Computational modeling of electrocardiograms: repolarization and T-wave polarity in the human heart. Comp. Meth. Biomech. Biomed. Eng. 17, 986–996.

Hurtado, D.E., Henao, D., 2014. Gradient flows and variational principles for cardiac electrophysiology: toward efficient and robust numerical simulations of the electrical activity of the heart. Comp. Meth. Appl. Mech. Eng. 273, 238–254.

Keener, J., Sneyd, J., 2004. Mathematical Physiology. Springer Science and Business Media.

Klepach, D., Lee, L.C., Wenk, J.F., Ratcliffe, M.B., Zohdi, T.I., Navia, J.L., Kassab, G.S., Kuhl, E., Guccione, J.M., 2012. Growth and remodeling of the left ventricle: a case study of myocardial infarction and surgical ventricular restoration. Mech. Res. Comm. 42, 134–141.

Kotikanyadanam, M., Göktepe, S., Kuhl, E., 2010. Computational modeling of electrocardiograms – a finite element approach towards cardiac excitation. Int. J. Num. Meth. Biomed. Eng. 26, 524–533.

Krishnamoorthi, S., Sarkar, M., Klug, W.S., 2013. Numerical quadrature and operator splitting in finite element methods for cardiac electrophysilogy. Int. J. Num. Meth. Biomed. Eng. 29, 1243–1266.

Kumar, V., Abbas, A.K., Fausto, N., 2005. Robbins and Cotran Pathologic Basis of Disease. Elsevier Saunders.

Lee, L.C., Wenk, J.F., Zhong, L., Klepach, D., Zhang, Z.H., Ge, L., Ratcliffe, M.B., Zohdi, T.I., Hsu, E., Navia, J.L., Kassab, G.S., Guccione, J.M., 2013. Analysis of patient-specific surgical ventricular restoration: Importance of an ellipsoidal left ventricular geometry for diastolic and systolic function. J. Appl. Phys. 115, 136–144.

Markhasin, V.S., Solovyova, O., Katsnelson, L.B., Protsenko, Y., Kohl, P., Noble, D., 2003. Mechano-electric interactions in heterogeneous myocardium: development of fundamental experimental and theoretical models. Prog. Biophys. Mol. Biol. 82, 207–220.

Murtada, S.C., Arner, A., Holzapfel, G.A., 2012. Experiments and mechanochemical modeling of smooth muscle contraction: significance of filament overlap. J. Theor. Bio 297, 176–186.

Nagumo, J., Arimoto, S., Yoshizawa, S., 1962. An active pulse transmission line simulating nerve axon. Proc. Inst. Radio Eng. 50, 2061–2070.

Nash, M.P., Panfilov, A.V., 2004. Electromechanical model of excitable tissue to study reentrant cardiac arrhythmias. Progr. Biophys. Mol. Bio 85, 501–522.

Pezzuto, S., Ambrosi, D., Quarteroni, A., 2014. An orthotropic active-strain numerical model for the mechanics of the myocardium. Euro. J. Mech. A/Solids 48, 83–96.

Rausch, M.K., Kuhl, E., 2013. On the effect of prestrain and residual stress in thin biological membranes. J. Mech. Phys. Solids 61, 1955–1969.

Robers, W.J., Shapiro, E.P., Weiss, J.L., Buchalter, M.B., Rademakers, F.E., Weisfeldt, M.L., Zerhouni, E.A., 1991. Quantification of and correlation for left-ventricular systolic long-axis shortening by magnetic-resonance tissue tagging and slice isolation. Circulation 84, 721–731.

Rossi, S., Ruiz-Baier, R., Pavarino, L., Quarteroni, A., 2012. Orthotropic active strain models for the numerical simulation of cardiac biomechanics. Int. J. Num. Meth. Biomed. Eng. 28, 761–788.

Rossi, S., Lassila, T., Ruiz-Baier, R., Sequeira, A., Quarteroni, A., 2014. Thermodynamically consistent orthotropic activation model capturing ventricular systolic wall thickening in cardiac electromechanics. Euro. J. Mech. A/Solids 48, 129–142.

Shmukler, M., 2004. Density of Blood. The Physics Factbook.

Smith, B.W., 2004. Minimal haemodynamic modelling of the heart and circulation for clinical application (dissertation). University of Canterbury, Christchurch, New Zealand.

Trayanova, N.A., 2011. Whole-heart modeling: applications to cardiac electrophysiology and electromechanics. Circ. Res. 108, 113–128.

Trayanova, N.A., Constantino, J., Gurev, V., 2011. Electromechanical models of the ventricles. Am. J. Phys. Heart Circ. Phys. 301, H279–H286.

Tsamis, A., Bothe, W., Kvitting, J.P., Swanson, J.C., Miller, D.C., Kuhl, E., 2011. Active contraction of cardiac muscle: in vivo characterization of mechanical activation sequences in the beating heart. J. Mech. Behav. Biomed. Mat. 4, 1167–1176.

Walker, J.C., Ratcliffe, M.B., Zhang, P., Wallace, A.W., Fata, B., Hsu, E.W., Saloner, D., Guccione, J.M., 2005. MRI-based finite-element analysis of left ventricular aneurysm. Am. J. Physiol. Heart Circ. Physiol. 289, H692–H700.

Wong, J., Göktepe, S., Kuhl, E., 2013. Computational modeling of chemo-electro-mechanical coupling: a novel implicit monolithic finite element approach. Int. J. Num. Meth. Biomed. Eng. 29, 1104–1133.

Wong, J., Kuhl, E., 2014. Generating fiber orientation maps in human heart models using Poisson interpolation. Comp. Meth. Biomech. Biomed. Eng. 17, 1217–1226.

Zygote Media Group, Inc, 2013. The Zygote Solid 3D Heart Model.